Modeling Gas Effects in a Bubbling Fluidized Bed Reactor for Biomass Pyrolysis

Gavin M. Wiggins, Oluwafemi A. Oyedeji, and ?

September 7, 2020

Contents

Abstract

Fast pyrolysis of biomass in a fluidized bed reactor is typically conducted in a nitrogen gas environment. Recycling product gas can improve the economics of operating such a system by reducing reliance on pure process streams. However, almost no work has been performed to model the effects of carrier gas properties on fluidization characteristics and biomass devolatilization. Gas effects in a fluidized bed biomass pyrolysis reactor using engineering correlations, low-order models, and CFD simulations were investigated for N_2, H_2, H_2O, CO, CO_2, and CH_4 carrier gas mixtures. Our findings reveal viscosity of a gas mixture can be significantly underestimated depending on the model. Also, fluidization characteristics such as U_{mf} are greatly affected by gas properties but the effect on biomass pyrolysis yields is negligible.

1 Introduction

Fast pyrolysis is a versatile method for thermochemical conversion of solid biomass into liquid bio-oil which can be used for bio-fuel and high-value chemical production. Bio-oil is commonly generated in bubbling fluidized bed and circulating fluidized bed reactor systems in which biomass particles rapidly devolatilize in the absence of oxygen into mixtures of light gases, condensable bio-oil vapors, and solid char [4, 5, 20]. Since biomass pyrolysis normally occurs in a non-oxidizing environment, the fluidization gas (carrier gas) is often pure nitrogen [20]. To maximize bio-oil yields, the reactor typically operates at temperatures near 500°C and must maintain particle residence times up to 10 seconds and gas residence times less than 2 seconds [5]. Deviations from these conditions can result in significant production and quality penalties, therefore optimal reactor design and control become crucial to achieving commercially viable bio-oil production.

To improve the economic possibilities of biomass fast pyrolysis systems, char can be burned for process heat while recycled pyrolysis gas can assist with fluidization [4, 18]. The major generated components of pyrolysis gas are CO, CO_2, CH_4, H_2, along with other light hydrocarbons [1, 34]. Several experiments investigated the effects of these gases on reactor conditions and pyrolysis yields [18, 21, 34] but modeling the effects of the different gases was not discussed.

Autothermal pyrolysis experiments in a fluidized bed reactor have shown that the presence of oxygen in the carrier gas can prevent reactor clogging by reducing char formation [15]. The addition of oxygen can also improve heat transfer within the reactor via partial oxidiation of the pyrolysis products without significant decreases in bio-oil yield [27]. Substituting air for nitrogen gas allowed for higher superficial velocities which promoted elutriation of char from reactor experiments while having neglible effect on bio-oil yield [26]. Modeling the fluidization of the autothermal experiments was not discussed in the available literature.

There are several fluidized bed reactor models that investigate the hydrodynamics and conversion of biomass at fast pyrolysis conditions [25, 24, 19, 31, 32]. These models assume the carrier gas is pure nitrogen which is a typical scenario for biomass fast pyrolysis. The authors are not aware of any models in the biomass pyrolysis literature that investigate the effects of a carrier gas other than pure nitrogen.

This paper uses engineering correlations, reduced-order modeling techniques, and CFD simulations to model a bubbling fluidized bed pyrolysis reactor. The models are used to evaluate different fluidization gases and their effects on the hydrodynamics and biomass conversion in a fluidized bed reactor operating at fast pyrolysis conditions.

2 Experimental apparatus

The NREL 2FBR reactor system thermochemically converts biomass feedstock at fast pyrolysis conditions. The system is comprised of two bubbling fluidized bed (BFB) reactors where the first reactor is for biomass fast pyrolysis and the second reactor is for vapor phase upgrading. Yields from the BFB pyrolysis reactor are compared to model results discussed later in this paper.

An overview of the NREL 2FBR system is shown in Figure 1, components of the pyrolysis reactor are detailed in Figure 2, while dimensions and typical operating conditions of the pyrolysis unit are given in Figure 3. Sand is used as the dominant heat transfer medium in the pyrolyzer. Biomass particles are fed to the reactor via a screw auger and nitrogen is used as the fluidization/carrier gas. More information about the NREL 2FBR biomass pyrolysis system is available elsewhere [14, 29].

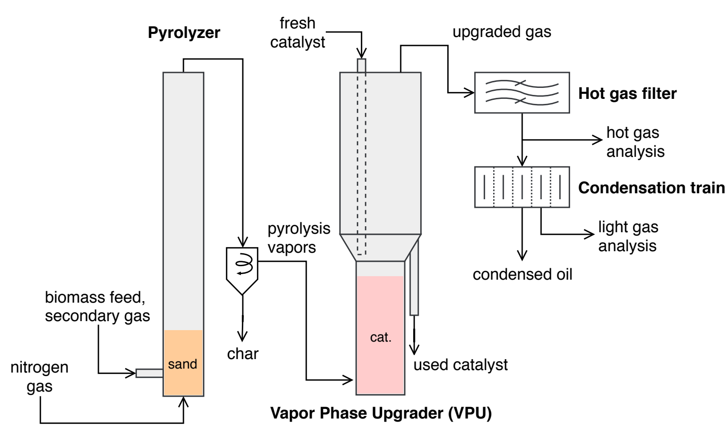

Figure 1: Overview of the NREL 2FBR system. Biomass fast pyrolysis occurs in the pyrolyzer (left) and gaseous products are catalytically upgraded in the vapor phase upgrader (right).

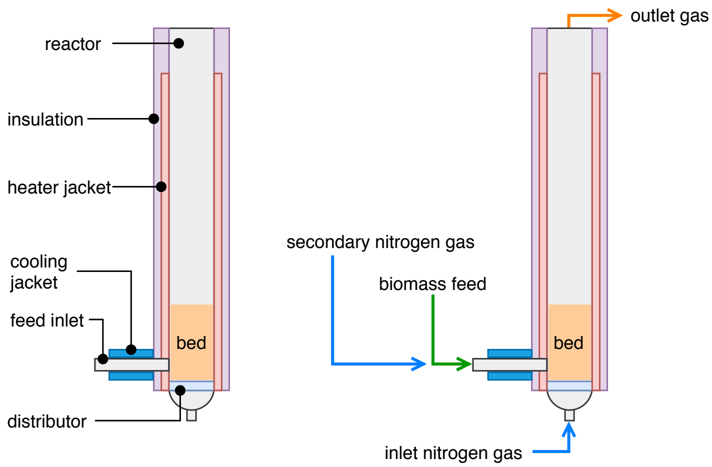

Figure 2: Components of the BFB biomass pyrolysis reactor referred to as the "pyrolyzer" in the NREL 2FBR system.

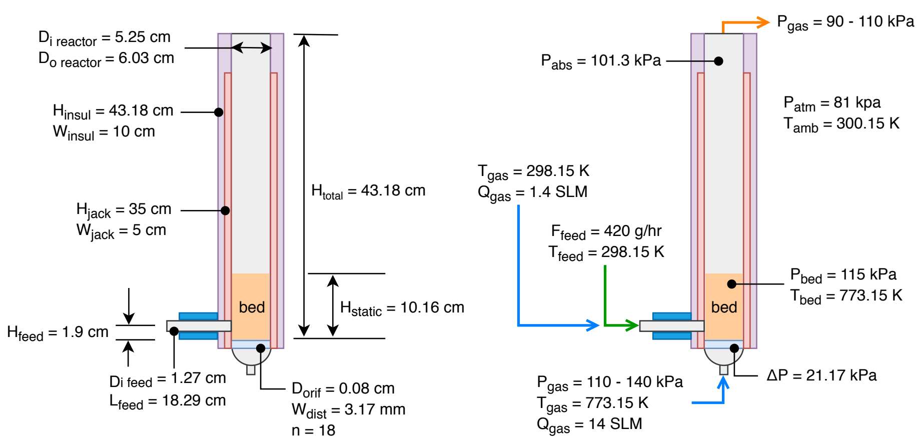

Figure 3: Dimensions and typical fast pyrolysis operating conditions for the BFB biomass pyrolysis reactor in the NREL 2FBR system.

3 Modeling approach

Gas property equations along with models for calculating viscosity of a gas mixture are discussed in the following sections. Fluidization correlations relevant to bubbling fluidized bed reactors are also discussed. An overview of the biomass pyrolysis kinetics scheme is given and dimensionless numbers for understanding the controlling mechanisms for the problem are examined. Finally, equations pertaining to the CFD-DEM simulations are discussed.

3.1 Gas properties

Density of the gas is calculated from the ideal gas law as shown in Equation 1 where ρ_{gas} is density (kg/m^3), P is pressure (Pa), M is molecular weight (g/mol), R is the gas constant [(m^3 Pa) / (K mol)], and T is temperature (K).

$$\rho_{\mathrm{gas}} = \frac{P\,M}{R\,T} \tag{1}$$

Gas viscosity (μ_{gas} as µP) is determined from Equation 2, thermal conductivity (k_{gas} as W/m K) is estimated from Equation 3, and heat capacity ($\mathrm{C}_{p\,gas}$ as J/mol K) is calculated from Equation 4. Temperature of the gas in Kelvin is represented by T while the regression coefficients A, B, C, D, E, F, and G for each gas are obtained from Yaws' Handbook [33].

$$\mu_{\mathrm{gas}} = A + B\,T + C\,T^2 + D\,T^3 \tag{2}$$

$$k_{\mathrm{gas}} = A + B\,T + C\,T^2 + D\,T^3 \tag{3}$$

$$C_{\mathrm{p\,gas}} = A + B\,T + C\,T^2 + D\,T^3 + E\,T^4 + F\,T^5 + G\,T^6 \tag{4}$$

Several methods are available to calculate the dynamic viscosity of a gas mixture. The simplest approach is Graham's model in Equation 5 which sums the gas viscosities (μ_i) and mole fractions (x_i) of each component [12].

$$\mu_{\mathrm{mix}} = \sum (x_i\;\mu_i) \tag{5}$$

The Herning and Zipperer approach shown by Equation 6, sums the viscosities weighted by the square root of the molecular weight (M_i) for each component [13]. According to Davidson's report [8], this model is not recommended for gas mixtures containing significant amounts of hydrogen.

$$\mu_{\mathrm{mix}} = \sum \frac{\mu_i\;x_i\;\sqrt{M_i}}{x_i\;\sqrt{M_i}} \tag{6}$$

Wilke's model represented by Equations 7 and 8 is based on a kinetic theory implementation which requires a coefficient (ϕ_{ij}) for each gas component [30]. The coefficients are used along with the mole fractions to calculate the overall mixture viscosity.

$$\phi_{ij} = \frac{\left[1 + (\mu_i/\mu_j)^{1/2}(M_j/M_i)^{1/4}\right]^2}{(4/\sqrt{2})\left[1 + (M_i/M_j)\right]^{1/2}} \tag{7}$$

$$\mu_{\mathrm{mix}} = \sum_{i=1} \frac{\mu_i}{1 + \frac{1}{x_i}\sum_{\substack{j=1\\ j\neq i}} x_j\,\phi_{ij}} \tag{8}$$

Brokaw provides a model for nonpolar and polar gas mixtures that utilizes the viscosities, molecular weights, and mole fractions of the mixture components [6]. The molecular weight ratios of the gas components are described by Equations 9 and 10; the ratios are used in Equation 11 to calculate the overall mixture viscosity where $S_{ij} = 1$ for nonpolar gases.

$$m_{ij} = \left[4 M_i M_j / (M_i + M_j)^2\right]^{1/4} \tag{9}$$

$$A_{ij} = m_{ij} \left(\frac{M_j}{M_i}\right)^{1/2} \left[1 + \frac{\frac{M_i}{M_j} - \left(\frac{M_i}{M_j}\right)^{0.45}}{2\left(1 + \frac{M_i}{M_j}\right) + \frac{1+\left(\frac{M_i}{M_j}\right)^{0.45}}{1+m_{ij}} m_{ij}}\right] \tag{10}$$

$$\mu_{\text{mix}} = \sum_{i=1} \frac{x_i \sqrt{\mu_i}}{\frac{x_i}{\sqrt{\mu_i}} + \sum_{\substack{j=1 \\ j\neq i}} \frac{S_{ij}\, A_{ij}}{\sqrt{\mu_j}} x_j} \tag{11}$$

The approach by Davidson estimates viscosity in terms of the fluidity of the gas mixture [8]. This method utilizes the momentum efficiency of the gas components to predict the mixture fluidity which is the reciprocal of the gas viscosity as given by Equations 12, 13, and 14 respectively. The empirical constant A was calculated as 0.375 using reported viscosities of 35 gas pairs [8].

$$E_{ij} = \frac{2\sqrt{M_i\, M_j}}{M_i + M_j} \tag{12}$$

$$f = \sum \frac{x_i\, x_j}{\sqrt{\mu_i\, \mu_j}} E_{ij}^A \tag{13}$$

$$\mu_{\text{mix}} = 1/f \tag{14}$$

3.2 Fluidization correlations

For a bed of particles, the minimum fluidization velocity U_{mf} is the gas velocity at which the drag force of the upward moving gas equals the weight of the particles. Kunii and Levenspiel [16] provide the following equation for calculating minimum fluidization velocity

$$U_{\text{mf}} = \frac{Re_{\text{p,mf}}\, \mu}{d_p\, \rho_g} \tag{15}$$

where μ is gas viscosity (kg/m s), d_p is particle diameter (m), ρ_g is gas density (kg/m^3), and $Re_{p,mf}$ is the particle Reynolds number (-) at minimum fluidization conditions. The Reynolds number is calculated from the Archimedes number (Ar) and two dimensionless constants (a, b) which represent experimental coefficients. Different U_{mf} correlations were evalutaed based on experimental data from Wen and Yu where $(a, b) = (33.7, 0.0408)$, from Richardson where $(a, b) = (25.7, 0.0365)$, and from Grace where $(a, b) = (27.2, 0.0408)$ [16].

$$Re_{p,mf} = \left(a^2 + bAr\right)^{1/2} - a \tag{16}$$

$$Ar = \frac{d_p^3 \rho_g (\rho_s - \rho_g) g}{\mu^2} \tag{17}$$

According to Kunii and Levenspiel [16], the constants (a, b) can be derived from the Ergun pressure drop equation based on the constants K_1 and K_2 where ϵ_{mf} is the bed void fraction (-) at minimum fluidization and ϕ is sphericity (-) of the bed particles. For this paper, U_{mf} is estimated based on the Ergun, Grace, Richardson, and Wen and Yu correlations.

$$a = \frac{K_2}{2K_1} \qquad b = \frac{1}{K_1} \tag{18}$$

$$K_1 = \frac{1.75}{\epsilon_{mf}^3 \phi} \qquad K_2 = \frac{150(1 - \epsilon_{mf})}{\epsilon_{mf}^3 \phi^2} \tag{19}$$

As shown in Equation 20, the convective heat transfer coefficient h in W/m^{2}K can be determined from the Nusselt number Nu where Re is the Reynolds number, d_p is the biomass particle diameter, d_b is the sand particle diameter, and k_g is the gas thermal conductivity W/mK; valid for $d_p < d_b$ [7]. The Reynolds number is determined from ρ which is the gas density in kg/m^3, the minimum fluidization velocity U_{mf} in m/s, and the gas viscosity μ in kg/m s [24].

$$Nu = 2 + 0.9\, Re^{0.62} \left(\frac{d_p}{d_b}\right)^{0.2} = \frac{h\, d_p}{k_g} \tag{20}$$

$$Re = \frac{\rho\, U_{mf}\, d_p}{\mu} \tag{21}$$

$$\tag{22}$$

3.3 Dimensionless numbers

As mentioned in the work of Pyle and Zaror [28], the rate of pyrolysis involves a balance between internal and external heat transfer due to heat transport and reaction. This balance is embodied by the dimensionless numbers Bi, Py$^{\mathrm{I}}$, and Py$^{\mathrm{II}}$ which are determined from Equations 23, 24, and 25 respectively. The Biot number Bi represents the ratio of convective and conductive heat transport. The first pyrolysis number Py$^{\mathrm{I}}$ demonstrates the ratio of heat transfer by conduction to the rate of heat loss due to products leaving the particle. The second pyrolysis number Py$^{\mathrm{II}}$ reflects the effect of convective heat transfer to the external particle surface relative to the reaction heat loss. The Biot and pyrolysis numbers are calculated using the following parameters: h is the convective heat transfer coefficient in W/m^{2}K, R is the radius or characteristic length of the biomass particle in meters, k is the biomass thermal conductivity in W/mK, ρ is the density of the biomass particle in kg/m^3, K is the total rate constant in 1/s for the primary reactions, and C_p is the biomass heat capacity calculated from $103.1 + 3.867\,T$ where T is the biomass temperature in Kelvin.

$$Bi = \frac{h\,R}{k} \tag{23}$$

$$Py^{\mathrm{I}} = \frac{k}{\rho\, C_p\, R^2\, K} \tag{24}$$

$$Py^{\mathrm{II}} = \frac{h}{\rho\, C_p\, R\, K} \tag{25}$$

The Prandtl number is a dimensionless number representing the ratio of momentum diffusivity to thermal diffusivity. It is calculated from the equation shown below where C_p is heat capacity (J/kg·K), μ is dynamic gas viscosity (kg/m·s), and k is thermal conductivity (W/m·K).

$$Pr = \frac{C_p\, \mu}{k} \tag{26}$$

3.4 Biomass pyrolysis kinetics

A pyrolysis kinetics scheme based on the work of Di Blasi was implemented to predict the conversion of biomass into gas, tar, and char products [2, 3]. Figure 4 gives an overview of the scheme and its reaction mechanisms. Reactions 1–3 represent the primary conversion of biomass while reactions 4–5 are secondary reactions that reduce tar yield at long residence times.

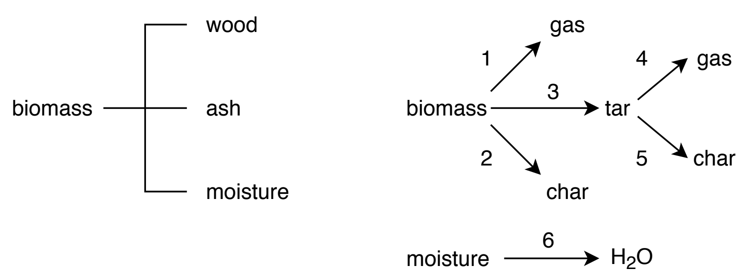

Figure 4: Diagram of the Di Blasi pyrolysis kinetics scheme for conversion of biomass to gas, tar, and char products.

The pyrolysis reactions were modeled as first-order Arrhenius type equations where the reaction rate is given as

$$r_i = C_i\, A_i\, e^{-E_i/R\,T} \tag{27}$$

where r_i is the rate of reaction i such that C_i is a mass based concentration, A_i is the pre-factor (1/s), E_i is the activation energy (kJ/mol), R is the gas constant, and T is the reaction temperature (K). Kinetic parameters for each reaction are listed in Table 1 where ΔH is the heat of reaction (kJ/kg).

Table 1: Kinetic parameters for the Di Blasi biomass pyrolysis scheme.

Reaction	A (1/s)	E (kJ/mol)	ΔH (kJ/kg)	Reference
1	4.38×10^{9}	152.7	-20	[3]
2	3.27×10^{6}	111.7	-20	[3]
3	1.08×10^{10}	148.0	255	[3]
4	4.28×10^{6}	108.0	-42	[2]
5	1.00×10^{6}	108.0	-42	[2]
6	5.13×10^{6}	87.6	2700	?

3.5 CFD-DEM simulation

A coarse-grained CFD-DEM model was implemented for biomass pyrolysis in MFiX, an open-source, Fortran-based code [X]. The implemented coarse-grained CFD-DEM model in this research is an extension of the standard MFiX release. Gas phase transport was described using conservation equations of mass, momentum, energy, and chemical species in the Eulerian framework (Equations 28–31, respectively).

$$\frac{d(\epsilon_g \rho_g)}{dt} + \nabla(\epsilon_g \rho_g u_g) = S_\rho \tag{28}$$

$$\frac{d(\epsilon_g \rho_g u_g)}{dt} + \nabla(\epsilon_g \rho_g u_g u_g) = -\epsilon_g \nabla p + \nabla(\epsilon_g \tau) + \epsilon_g \rho_g g + S_u \tag{29}$$

$$\frac{d(\epsilon_g \rho_g E)}{dt} + \nabla(\epsilon_g \rho_g u_g E) = -\nabla Q + S_E \tag{30}$$

$$\frac{d(\epsilon_g \rho_g Y_i)}{dt} + \nabla(\epsilon_g \rho_g u_g Y_i) = -\nabla(D_i \nabla Y_i) + S_{Y_i} \tag{31}$$

where ϵ_g, ρ_g, u_g, p, τ, Q, and Y_i are gas phase volume fraction, density, velocity, pressure, stress tensor, conductive heat flux, and ith chemical species, respectively, t is time, g is acceleration due to gravity, D_i is mass diffusion coefficient for species, S_ρ, S_u, S_E, and S_{Y_i} are mass, momentum, energy, and chemical species source terms, respectively. Fixed quantities of discrete particles with identical initial conditions were lumped into a computational coarse-grained parcel (CGP), whose motion was governed by Newton's second law of motion. All particle forces and contact dynamics were calculated on the parcel scale, whereas heat and mass transfers were calculated on particle scale and projected to the entire parcel. Accordingly, all particles in same coarse- grained parcel possess identical temperature, chemical species concentration, and momentum. The mass and diameter of each coarse-grained parcel was such that:

$$m_{CGP} = m_p W \tag{32}$$

$$d_{CGP} = d_p W^{1/3} \tag{33}$$

where m_{CGP} is CGP mass, m_p is distinct particle mass, W parcel statistical weight, d_{CGP} is CGP diameter, and d_p is distinct particle diameter. Instantaneous accelerations (translational and rotational) for each coarse-grained parcel were calculated as:

$$\frac{du_{CGP}}{dt} = g - \frac{F_p}{m_{CGP}} + \frac{F_c}{m_{CGP}} + \frac{F_d}{m_{CGP}} \tag{34}$$

$$\frac{d\omega_{CGP}}{dt} = \frac{T_{CGP}}{I_{CGP}} \tag{35}$$

where u_{CGP} and ω_{CGP} are the CGP translational and rotational velocities, g is acceleration due to gravity, m_{CGP} is CGP mass, T_{CGP} is net torque on the CGP, and I_{CGP} is CGP moment of inertia. The term F_p represents pressure gradient force and is calculated as product of the CGP volume and pressure gradient. The CGP collision forces F_C (parcel-parcel and parcel-wall collisions) was modeled according linear spring-dashpot model [22]. Since the number of CGP collisions is significantly lower than the number of collisions expected in system with distinct particles, the CGP coefficient of restitution was modified as a correction for energy dissipations during collisions. The proposed modification to the CGP coefficient of restitution is calculated following kinetic theory of granular flow [17] as:

$$e_{CGP} = \sqrt{1 + (e_p^2 - 1)W^{1/3}} \tag{36}$$

where e_{CGP} is CGP coefficient of restitution and e_p is distinct particle coefficient of restitution. Two different drag models were used to estimate CGP drag force F_d based on well-documented difference in the fluidization behavior of sand and biomass in the literature [23]. Drag force was estimated following Ganser-corrected Gidaspow drag model for sand (bed material) particles and a filtered drag model for biomass particles. Th Ganser correction [9] was coupled to the Gidaspow model [11] to account for non-sphericity of the sand particles as expressed below:

$$\beta_{Ganser} = \begin{cases} \beta_{Ergun} & \text{if } \epsilon_g \leq 0.8 \\ \beta_{WenYu} & \text{if } \epsilon_g > 0.8 \end{cases} \tag{37}$$

$$\beta_{Ergun} = 150 \frac{(1-\epsilon_g)^2 \mu_g}{\epsilon_g d_{CGP}^2 \phi^2} + 1.75 \frac{(1-\epsilon_g)\rho_g}{\epsilon_g d_{CGP} \phi} |u_g - u_{CGP}| \tag{38}$$

$$\beta_{WenYu} = \frac{3}{4} C_d \frac{(1-\epsilon_g)\rho_g}{d_{CGP}\phi} |u_g - u_{CGP}| \epsilon_g^{-2.65} \tag{39}$$

$$C_d = \begin{cases} \frac{24}{ReK_1}(1+0.1118(ReK_1K_2)^{0.6567}) + \frac{0.4305K_2}{1+\frac{3305}{ReK_1K_2}} & \text{if } Re < 1,000 \\ 0.44 & \text{if } Re \geq 1,000 \\ 0.0 & \text{if } Re = 0.0 \end{cases} \tag{40}$$

$$K_1 = \left(\frac{1}{3} + \frac{2}{3}\phi^{-0.5}\right)^{-1} - 2.25\frac{d_{CGP}}{D} \tag{41}$$

$$K_2 = 10^{1.8148(-log\phi)^{0.5743}} \tag{42}$$

The filtered drag model (modified Sarkar drag model) used in this research for biomass particles was proposed by Gao et al. [10] and was found by the authors to have relatively high prediction strength across multiple flow regimes in fluidized bed. The modified Sarkar drag model is derived fine-grid simulation with Wen-Yu drag model and can be computed as:

$$\beta_{Sarkar} = \beta_{WenYu}(1 - H_{Sakar}) \tag{43}$$

$$H_{Sakar} = \begin{cases} 0.95\left(1 - e^{-\alpha_1\alpha_2(u^*_{\text{slip}}-u_0)^p}\right) & u^*_{\text{slip}} > u_0 \\ 0.0 & u^*_{\text{slip}} \leq u_0 \end{cases} \tag{44}$$

$$u^*_{\text{slip}} = \frac{|u_g - u_{CGP}|}{u_t} \tag{45}$$

$$\alpha_1 = \frac{\left(a_1 + a_2(1-\epsilon_g) + a_3(1-\epsilon_g)^2 + a_4(1-\epsilon_g)^3 + a_5(1-\epsilon_g)^4\right)}{1 + e^{100((1-\epsilon_g)-0.55)}} \tag{46}$$

$$\alpha_2 = \left(1 + \frac{a_6}{\Delta^*_{\text{filter}}} + \frac{a_7}{(\Delta^*_{\text{filter}})^2}\right)\left(1 + \frac{a_8}{(u^*_{\text{slip}})^2}\right) \tag{47}$$

$$u_0 = \frac{a_9 + a_{10}(1-\epsilon_g)}{0.01 + (1-\epsilon_g)^{a_{11}}}\left(1 + \frac{a_{12}}{\Delta^*_{\text{filter}}} + \frac{a_{13}}{(\Delta^*_{\text{filter}})^2}\right) \tag{48}$$

$$p = \left(a_{14} + a_{15}(1-\epsilon_g) + a_{16}(1-\epsilon_g)^2\right)\left(1 + \frac{a_{17}}{\Delta^*_{\text{filter}}} + \frac{a_{18}}{(\Delta^*_{\text{filter}})^2}\right) \tag{49}$$

$$\Delta^*_{\text{filter}} = max\left(\frac{g\Delta_{\text{filter}}}{u_t^2}, \frac{1}{2}\right) \tag{50}$$

$$\Delta_{\text{filter}} = 2(\Delta_x \times \Delta_y \times \Delta_z)^{1/3} \tag{51}$$

$$u_t = \frac{gd^2_{CGP}(\rho_{CGP} - \rho_g)}{18\mu_g} \tag{52}$$

$$
\begin{matrix} a_1 & a_2 & a_3 \\ a_4 & a_5 & a_6 \\ a_7 & a_8 & a_9 \\ a_{10} & a_{11} & a_{12} \\ a_{13} & a_{14} & a_{15} \\ a_{16} & a_{17} & a_{18} \end{matrix} = \begin{matrix} 0.75597773 & 2.73931487 & -5.60196497 \\ -1.65853820 & 16.70299223 & -0.44145335 \\ 0.18195034 & -0.01827347 & 0.28441799 \\ -1.943573770 & 0.22177961 & 0.31175890 \\ -0.15971960 & 0.47750002 & 0.062794180 \\ 5.13011673 & 0.67680355 & -0.54535726 \end{matrix} \tag{53}
$$

4 Model parameters

Parameters for the reduced-order model and CFD simulations are provides in Tables 2 and 3. Biomass particle characteristics and properties are representative of loblolly pine. Bed particle characteristics are for typical sand material. Operating conditions and reactor dimensions are based on the previously discussed NREL 2FBR fluidized bed pyrolysis unit.

Table 2: Particle size distribution for biomass feedstock.

Sauter mean diameter (μm)	Mass fraction (%)	Mass flow rate (kg/hr)
278	12.1	0.018
344	51.0	0.076
426	34.2	0.051
543	2.7	0.004

Table 3: Parameters for the biomass, sand (bed material), and reactor operation. Biomass C_p calculated from particle composition.

Parameter	Value	Description
biomass particle		
e_p	0.2	particle-particle coefficient of restitution
e_w	0.2	particle-wall coefficient of restitution
e_s	0.2	particle-sand coefficient of restitution
μ_p	0.1	particle-particle coefficient of friction
μ_w	0.2	particle-wall coefficient of friction
μ_s	0.1	particle-sand coefficient of friction
k_n	100 N/m	particle spring constant
sand particle		
d_p	453 μm	particle diameter
ρ_p	2500 kg/m^3	particle density
C_p	830 kJ/(kg K)	particle heat capacity
ϕ	0.94	particle sphericity
e_p	0.61	particle-particle coefficient of restitution
e_w	0.61	particle-wall coefficient of restitution
μ_p	0.1	particle-particle coefficient of friction
μ_w	0.2	particle-wall coefficient of friction
k_n	100 N/m	particle spring constant
reactor operation		
d_{inner}	5.25 cm	inner reactor diameter
H_{reactor}	43.18 cm	reactor height
H_{static}	10.16 cm	static bed height
p_{gas}	101.325 kPa	gas pressure
T_{gas}	773.15 K	gas temperature
Q_{gas}	14 SLM	inlet gas flowrate

Table 4 represents the CFD simulations conducted for this paper. Each row is for a different simulation case which is performed for a particular gas composition.

Table 4: Simulation cases for different gas mixtures where columns denote gas percentage.

Case	N_2	H_2	H_2O	CO	CO_2	CH_4
1	100	0	0	0	0	0
2	0	100	0	0	0	0
3	0	0	100	0	0	0
4	0	0	0	100	0	0
5	0	0	0	0	100	0
6	0	0	0	0	0	100
7	20	20	0	20	20	20
8	50	0	0	0	50	0
9	50	0	0	50	0	0
10	0	0	50	50	0	0
11	100	0	0	0	0	0
12	80	20	0	0	0	0
13	60	40	0	0	0	0
14	50	50	0	0	0	0
15	40	60	0	0	0	0
16	30	70	0	0	0	0
17	20	80	0	0	0	0
18	15	85	0	0	0	0
19	10	90	0	0	0	0
20	5	95	0	0	0	0
21	0	100	0	0	0	0

Table 5: Chemical species composition of biomass feedstock.

Species	Mass fraction (%)	Density (kg/m^3)
moisture	4.0	1,000
wood	95.9	500
ash	0.1	2,000
char	0.0	300

Table 6: Simulation parameters settings.

Parameter	Value
CFD cell size, $\Delta_x \times \Delta_y \times \Delta_z$ (mm)	$4.3 \times 4.4 \times 4.3$
time step, Δ_x (s)	varies
biomass parcel statistical weight	10
sand parcel statistical weight	20
gas phase equation of state	ideal

Table 7: Simulation cases for different gas mixtures. Columns denote gas flow rate in m^3/s at 500°C. Additional 2.83×10^{-5} m^3/s of N_2 at 500°C supplied at fluidizing gas inlet for all cases. Additional 2.55×10^{-5} m^3/s of N_2 at 25°C supplied at biomass feed inlet for all cases.

ID	Case	N_2	H_2	H_2O	CO	CO_2	CH_4
0	N_2	6.56e-04	0	0	0	0	0
0	H_2	0	6.37e-04	0	0	0	0
0	H_2O	0	0	6.37e-04	0	0	0
0	CO	0	0	0	6.37e-04	0	0
0	CO_2	0	0	0	0	6.37e-04	0
0	CH_4	0	0	0	0	0	6.37e-04
0	N_2 + CO	3.18e-04	0	0	3.18e-04	0	0
0	N_2 + CO_2	3.47e-04	0	0	0	3.18e-04	0

5 Results and discussion

This section provides results and related discussions for the effects of different fluidization gases on the operation of a bubbling fluidized bed reactor. Gas effects on the pyrolysis yields of the biomass feedstock are also presented and discussed.

5.1 Pure gas properties

Molecular weight, viscosity, density, thermal conductivity, heat capacity, and Prandtl number of the individual gases investigated in this paper are shown in Figure 5. The gas properties were calculated at a pressure of 101,325 Pa and a temperature of 773.15 K (500°C). The lightest gas in terms of molecular weight and density is hydrogen while the heaviest gas is carbon dioxide. The highest viscosity is noted for the nitrogen gas while hydrogen has the lowest viscosity. The largest thermal conductivity is for hydrogen at approximately 0.36 W/(m K) while the other gases remain below 0.12 W/(m K). The highest heat capacity is obtained for methane at 62 J/(mol K) while the lowest is for hydrogen at 29 J/(mol K). The Prandtl number is similar for all the gases except for water vapor.

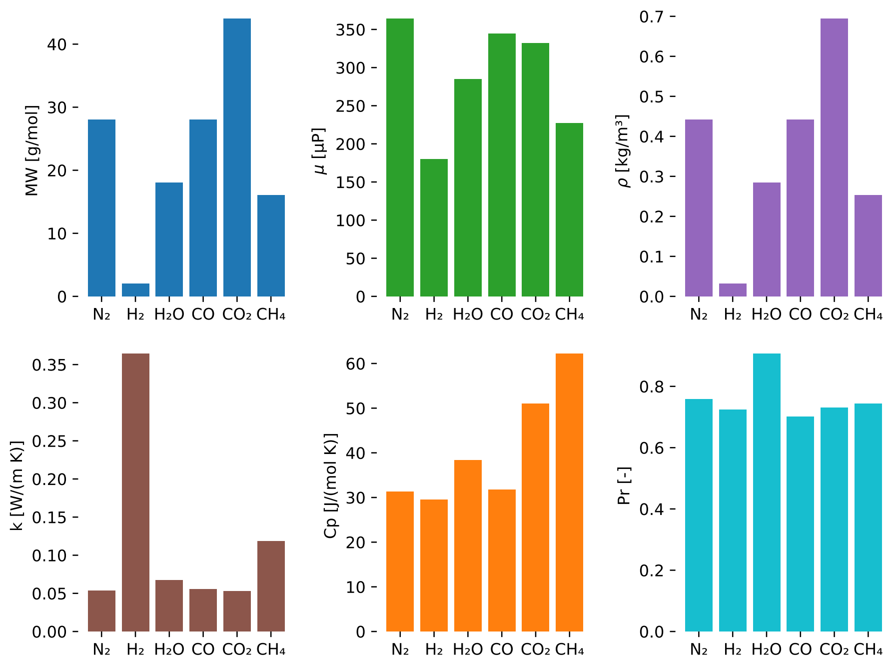

Figure 5: Comparison of molecular weight (MW), viscosity (μ), density (ρ), thermal conductivity (k), heat capacity (Cp), and Prandtl number (Pr) for each gas at 101,325 Pa and 773.15 K (500°C).

5.2 Gas mixture properties

Comparisons of the calculated viscosity of a H_2/N_2 gas mixture to measured values obtained from literature are shown in Figure 6. The models by Herning and Zipperer as well as Brokaw match well with the experimental data for a range of mixture ratios. This is contradictory to the Davidson report which does not recommend the Herning and Zipperer model for hydrogen mixtures [8]. The Davidson and Graham models significantly underpredict the mixture viscosity while the Wilke model tends to overestimate the viscosity. Similar results are obtained for a H_2/O_2 gas mixture as shown in Figure 7.

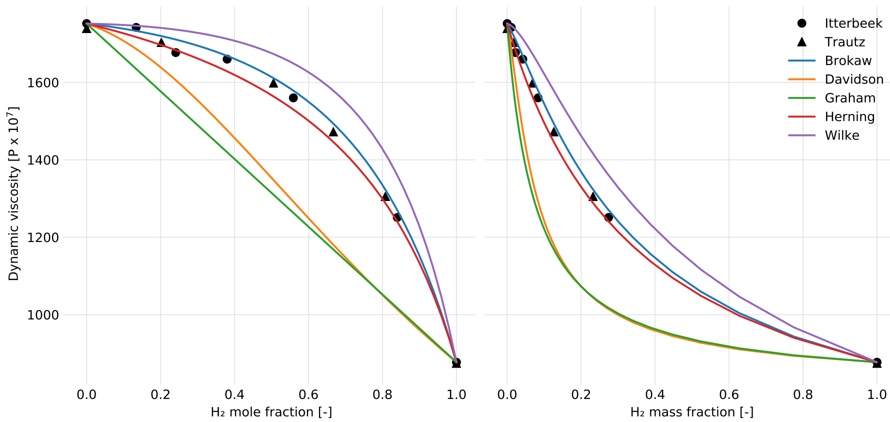

Figure 6: Viscosity of a H_2/N_2 mixture at 291.1 K (18°C). Calculated values represented by lines and measured values shown as symbols.

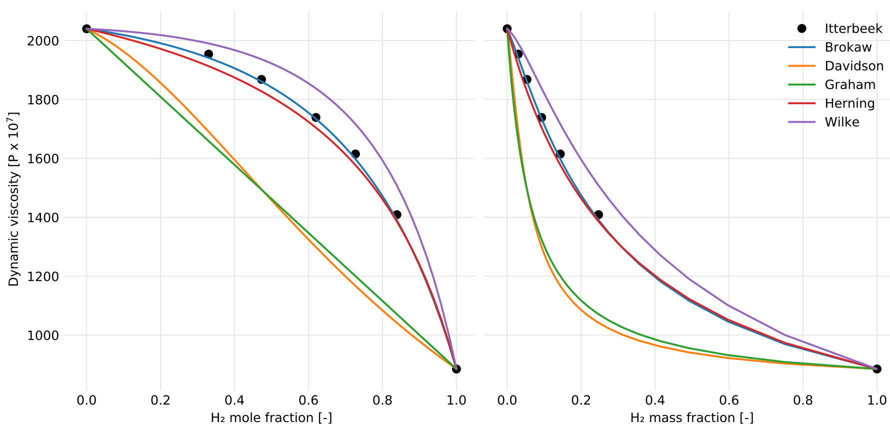

Figure 7: Viscosity of a H_2/O_2 mixture at 293.6 K (20°C). Calculated values represented by lines and measured values shown as symbols.

Properties for molecular weight, viscosity, and density for the gas mixtures investigated in this paper are shown in Figure 8. Similar to the individual gas properties, the mixture properties were calculated at 101,325 Pa and 773.15 K (500°C). The fraction of each gas in the mixture is given by the values shown at the top of each column in the figure. For example, the hydrogen and nitrogen mixture is comprised of 80% hydrogen and 20% nitrogen which is labeled as $0.8 + 0.2$. As expected, the carbon dioxide mixture is the heaviest in terms of molecular weight and density.

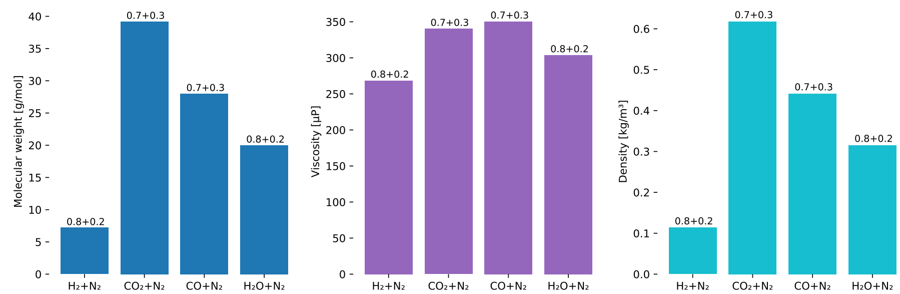

Figure 8: Comparison of gas mixture properties for molecular weight, viscosity, and density at 101,325 Pa and 773.15 K. Fraction of each gas component is shown at the top of each column.

5.3 Fluidization characteristics

Minimum fluidization velocity (Umf) of the bed material for the different fluidization gases is presented in Table 8. Hydrogen requires about twice the gas velocity to fluidize the bed of sand compared to the nitrogen, carbon monoxide, and carbon dioxide gases. This is due to hydrogen's lower viscosity and much lower density compared to the other gases. Water vapor and methane require moderately higher fluidization velocities compared to the nitrogen gas. A comparison of Umf for the various fluidization gases is displayed in Figure 9.

Table 8: Minimum fluidization velocity (m/s) of the bed material calculated from various correlations for different fluidization gases. Last row represents the average Umf value for each gas.

U_{mf}	N_2	H_2	H_2O	CO	CO_2	CH_4
Ergun	0.14	0.30	0.18	0.15	0.16	0.23
Grace	0.10	0.21	0.13	0.11	0.11	0.16
Richardson	0.10	0.20	0.12	0.10	0.11	0.15
Wen and Yu	0.08	0.17	0.11	0.09	0.09	0.13
average	0.11	0.22	0.14	0.11	0.12	0.17

The superficial gas velocity (U_s) of the nitrogen gas flow is calculated as 0.3072 m/s which is based on the 14 SLM gas flow through the distributor plate. Using this value, the ratio of Us to Umf is shown in Table 9 for different fluidization gases. The BFB pyrolysis reactor at NREL typically operates at a Us/Umf of 3 with nitrogen gas. For gases such as H_2, H_2O, CO, CO_2, and CH_4, the gas flow into the reactor must be increased to have similar fluidized bed characteristics as the nitrogen case. A comparison of the increased Us for each gas along with the associated Us/Umf is shown in Figure 10. As expected, the hydrogen gas flow must be approximately doubled compared to the nitrogen case to achieve similar fluidization of the bed material.

Table 9: Ratio of Us to Umf for different fluidization gases. Last row represents the average Us/Umf value for each gas.

U_s/U_{mf}	N_2	H_2	H_2O	CO	CO_2	CH_4
Ergun	2.13	1.04	1.67	2.02	1.97	1.34
Grace	2.99	1.47	2.35	2.84	2.76	1.88
Richardson	3.16	1.55	2.48	3.00	2.91	1.98
Wen and Yu	3.69	1.82	2.90	3.50	3.39	2.32
average	2.99	1.47	2.35	2.84	2.76	1.88

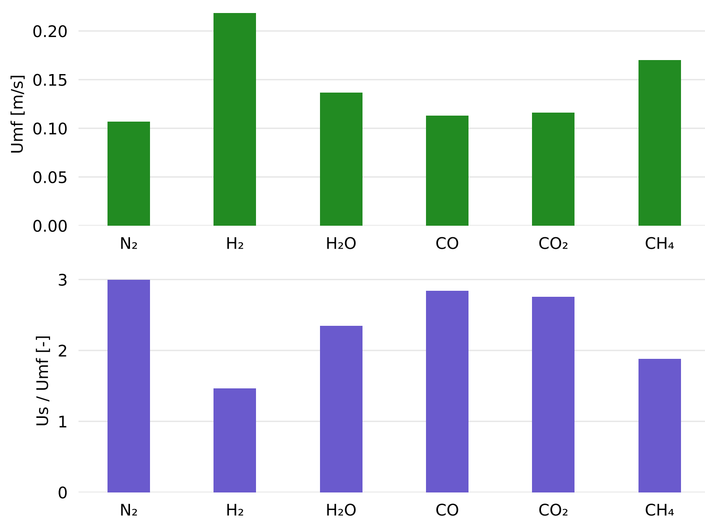

Figure 9: Comparison of the minimum fluidization velocity (Umf) and the ratio of Us/Umf for different fluidization gases. Superficial gas velocity is Us.

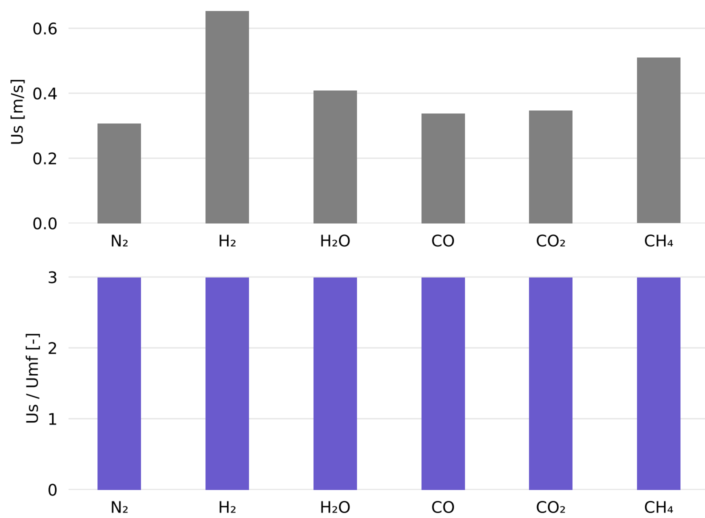

Figure 10: Comparison of the superficial gas velocity (Us) and the associated Us/Umf for different fluidization gases. Minimum fluidization velocity is Umf.

The Reynolds number was calculated using an average biomass particle diameter of 369.4 μm and the mean U_{mf} value. Next, the Nusselt number along with the associated convective heat transfer coefficient were calculated for each carrier gas as shown in Table 10 and Figure 11. The highest heat transfer coefficient is estimated for H_2 while the second highest result is for CH_4. This is largely due to the higher thermal conductivity of the hydrogen and methane compared to the other gases. Due to the higher heat transfer rate to the biomass particle in the hydrogen environment, one can expect the biomass to pyrolyze more quickly with the hydrogen carrier gas.

Table 10: Comparison of the Reynolds number, Nusselt number, and convective heat transfer coefficient (h) for different fluidization gases.

Gas	U_{mf}	Re	Nu	h
N_2	0.11	0.48	2.55	369.45
H_2	0.22	0.14	2.26	2224.25
H_2O	0.14	0.50	2.56	464.54
CO	0.11	0.53	2.58	389.53
CO_2	0.12	0.89	2.81	399.83
CH_4	0.17	0.70	2.69	862.61

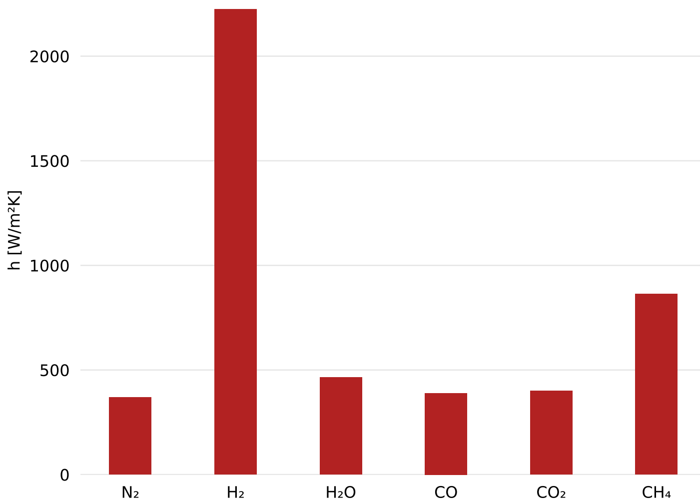

Figure 11: Convective heat transfer coefficient (h) for different fluidization gases. Values based on average biomass particle size and average minimum fluidization velocity.

5.4 Evaluation of the kinetic scheme

The Di Blasi kinetics were put to use in a batch reactor model to investigate the time scales associated with the reaction mechanisms. Figure 12 is an overview of the biomass conversion and product yields using the Di Blasi kinetics in a batch reactor at 773.15 K (500°C). At this temperature, without the effects of secondary reactions, the kinetics offer a maximum achievable tar yield of 78% within 5 seconds. However, if secondary reactions occur during the entire pyrolysis process then a maximum tar yield of only 53% is possible. The Di Blasi kinetics suggest that minimizing the extent of secondary reactions is critical to producing the maximum possible tar yield.

A range of reaction temperatures were applied to the Di Blasi kinetics in the batch reactor model as shown in Figure 13. The kinetics suggest that temperature has a neglible effect on primary tar yield but effects of secondary reactions are more pronounced. When secondary reactions occur during the entire pyrolysis process, maximum tar yields are realized at higher temperatures but with shorter residence times. These results suggest that if secondary reactions are minimized then temperature should not have a drastic effect on tar yield.

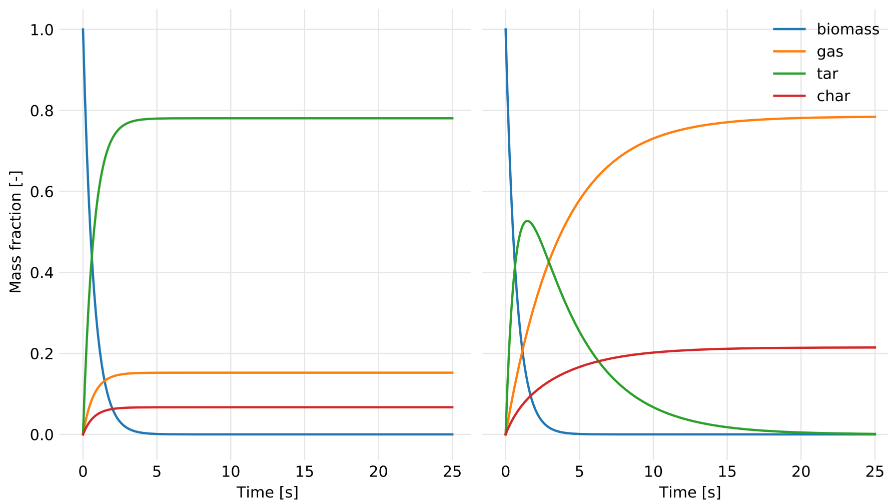

Figure 12: Biomass conversion and product yields in a batch reactor model at 773.15 K (500°C) according to the Di Blasi kinetic reactions. Results shown for primary reactions only (left) along with primary and secondary reactions (right).

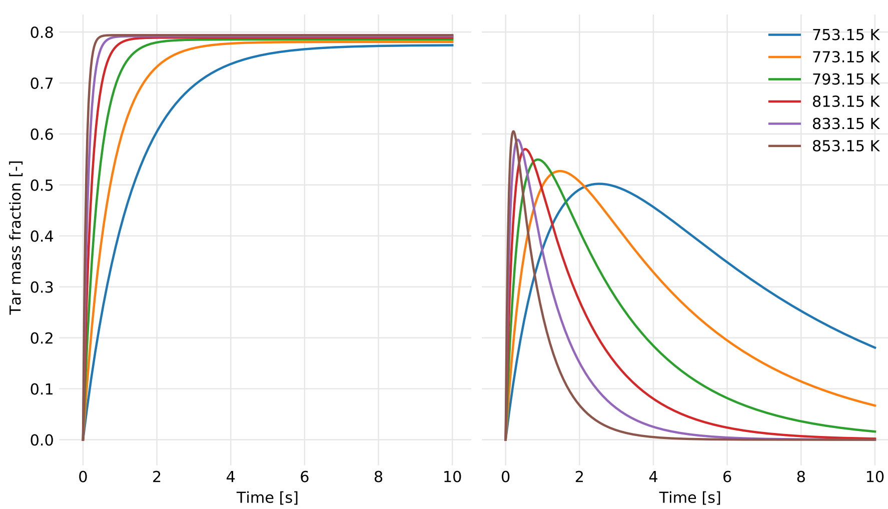

Figure 13: Tar yields for reaction temperatures of 753.15–853.15 K (480–580°C) using the Di Blasi kinetics in a batch reactor model. Results shown for primary tar (left) along with primary and secondary tar (right).

5.5 Limiting factors for biomass pyrolysis

Gas influence on the pyrolysis limiting regimes is shown in Figure 14 for a biomass particle diameter of 369.4 μm. The regime map suggests that gas properties have little effect on the limiting mode of pyrolysis. However, when comparing a range of particle diameters, the differences are more pronounced as seen in Figure 15. For larger particles, conduction becomes the limiting mode of pyrolysis especially for the hydrogen gas. For smaller particles, nitrogen gas promotes isothermal conditions along with a kinetically limited pyrolysis.

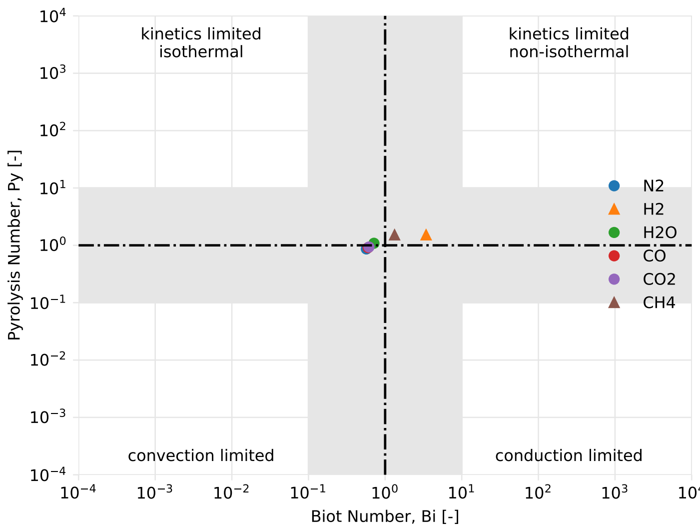

Figure 14: Comparison of carrier gas effects on pyrolysis regime for a 369.4 μm biomass particle.

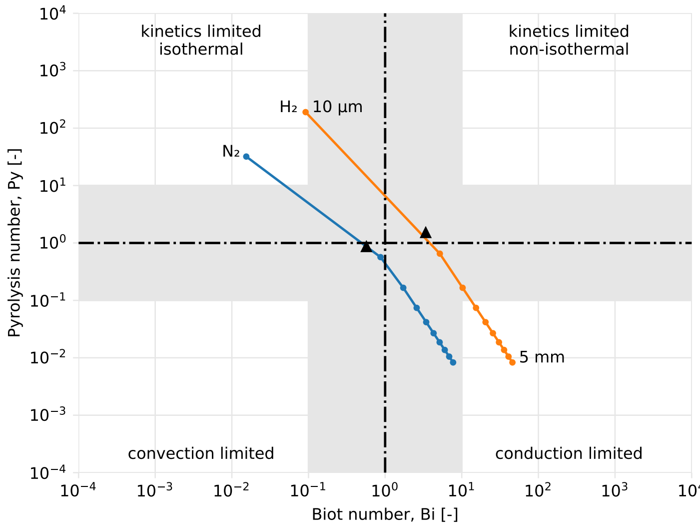

Figure 15: Comparison of nitrogen and hydrogen gas effects for biomass particles ranging from 10μm to 5 mm in diameter. Triangle markers symbolize 369.4 μm biomass particle diameter.

5.6 CFD-DEM validation

The predicted yield of pyrolysis products (bio-oil, light gas, and biochar) was validated against experimental data reported by [XXX]. In their experimental work, [XXX] carried out biomass pyrolysis in the same NREL 2FBR fast pyrolysis system that is modeled and simulated in this research. Additionally, the process variables used in the experimental work are consistent with those implemented for the N_2 and H_2 cases in this research. Figure 16 shows that the predicted yields of pyrolysis products closely follow the experimental data with absolute deviation ranging between 1% and 6%. The largest observed deviations occur in the prediction of bio-oil and are attributed to the non-closure of mass balance for the experimental data. The reported mass closure for the experimental data was about 94%. A mass-proportional adjustment of the experimental data to enforce 100% mass closure decreases the absolute deviation of bio-oil prediction to about 2% or less.

From a qualitative point of view, the implemented CFD-DEM simulation in this research was able to acceptably predict the increase in light gas yield and decrease in biochar yield when fluidizing gas was changed from N_2 to H_2, as seen in the experimental data. Predicted bio-oil yield slightly increased when fluidizing gas was changed from N_2 to H_2, contrary to experimental data showing a slight decrease. The relative change in bio-oil yield between N_2 to H_2 was however quite small for both experimental data (2%) and CFD-DEM prediction (-1%).

These results demonstrate that the CFD-DEM model implemented in this research is capable of realistically simulating the characteristic effects of fluidizing gas on the performance of lignocellulosic biomass pyrolysis.

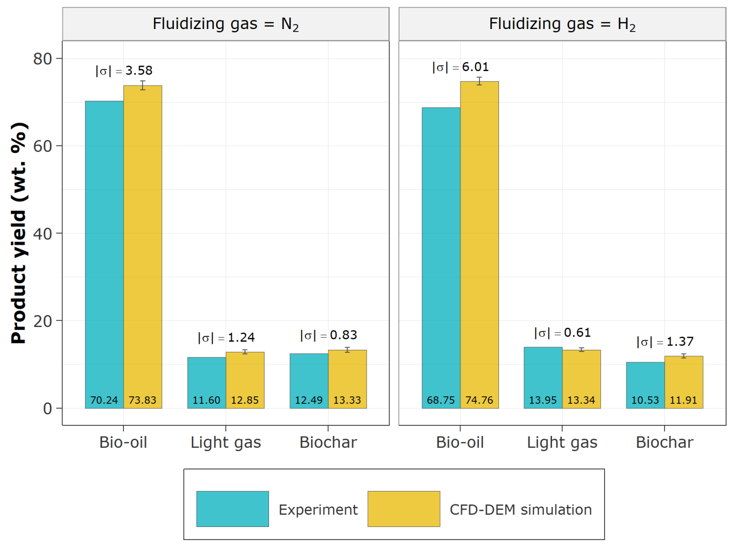

Figure 16: CFD-DEM simulation validation against experimental data. Product yields are calculated on a biomass basis. Deviation between experiment and simulation given by σ.

5.7 Fluidizing gas effect on pyrolysis performance

Figure 17 presents the volume-time averaged pressure drop and temperature along the height of the fluidized bed reactor. The different fluidizing gases considered in this research demonstrated similar effects on the pressure drop profile along the reactor height. Overall, the averaged bed height – as evidenced by the inflection point on the pressure drop curve – was about 0.14 m, regardless of fluidized gas. Similarly, the total pressure drop across the reactor was consistently about 1440 Pa for all fluidizing gases and mixtures. The volume-time averaged gas temperature ranged between 495°C and 500°C, depending on position along the reactor height and fluidizing gas. Gas temperature generally dipped around the biomass inlet and at the dense-bed/dilute- phase interface. The most noticeable trend in gas temperature occurs in the dilute-phase, with increasing gas temperature along the height of the reactor. Also noteworthy is the fact that gas temperature in the dilute-phase was highest when H_2 was used as fluidizing gas. This observation is attributable to the large difference in the thermal conductivity of H_2 and the other fluidizing gases (Figure XXX). The impact of the difference in the thermal conductivity of fluidizing gases is also evident in the average particle temperature and mass loss profile (Figure 18). When H_2 was used as fluidizing gas, biomass particles experienced significantly higher heating rate, and consequently higher mass loss rate, compared to when other fluidizing gases were used. Biomass heating and mass loss rate follow the order: H_2 > CH_4 > H_2O > CO_2 > N_2 + CO_2 > N_2 > N_2 + CO > CO, irrespective of the initial size of the biomass particle.

Furthermore, it was observed that tar conversion reactions (Reactions 4 and 5) slightly changed among fluidizing gas used, with the lowest being N_2 and the highest being H_2 (Figure 19). This observation explains the reason why despite H_2 yielded the highest particle heating and mass loss rate (Figure 18), and one of the longest residence times (Figure 20), its bio-oil yield relative to biomass flow rate is negligibly different from the bio-oil yield with other fluidizing gases, especially N_2. Nevertheless, the fact that we found that fluidizing gas can notably increase biomass heating and mass loss rate (pyrolysis conversion rate) suggest potential process intensification implication because increased heating and pyrolysis rate represents a system where pyrolysis can be completed at an increased rate and consequently offering increased system throughput. Our finding suggests that, at the least, fluidizing gas with produced light gases can be recirculated as fluidizing gas without detrimental consequences on pyrolysis performance.

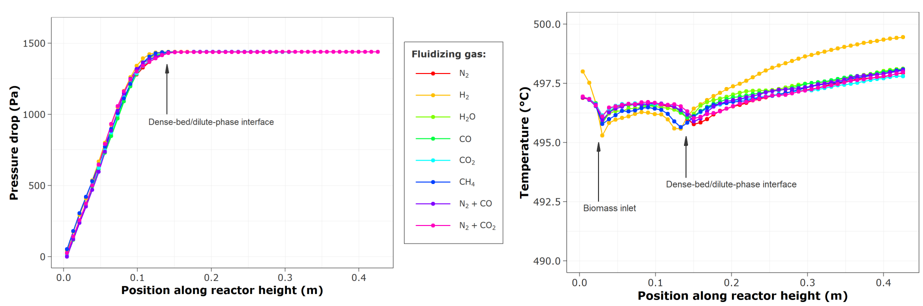

Figure 17: Time-averaged distribution of gas phase pressure drop (left) and temperature (right) along the reactor height.

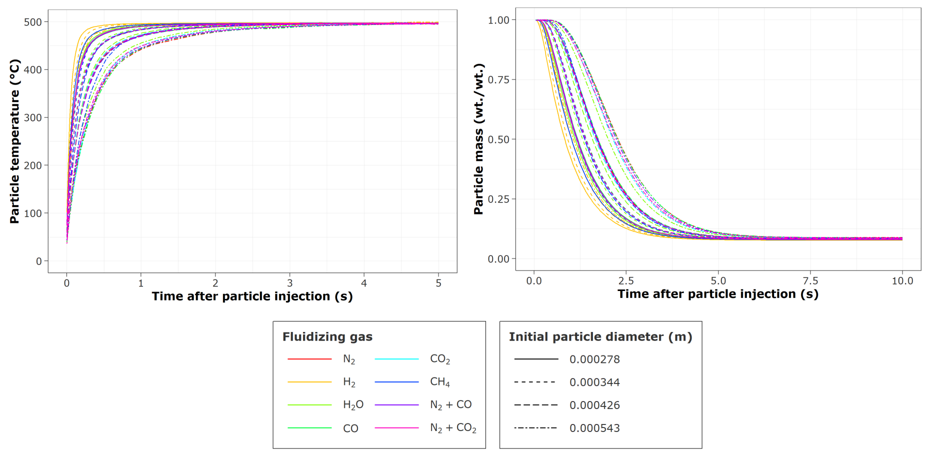

Figure 18: Average particle temperature (left) and mass loss (right) profile during pyrolysis. Line color discriminates among fluidizing gas, whereas line type discriminates among initial particle diameter.

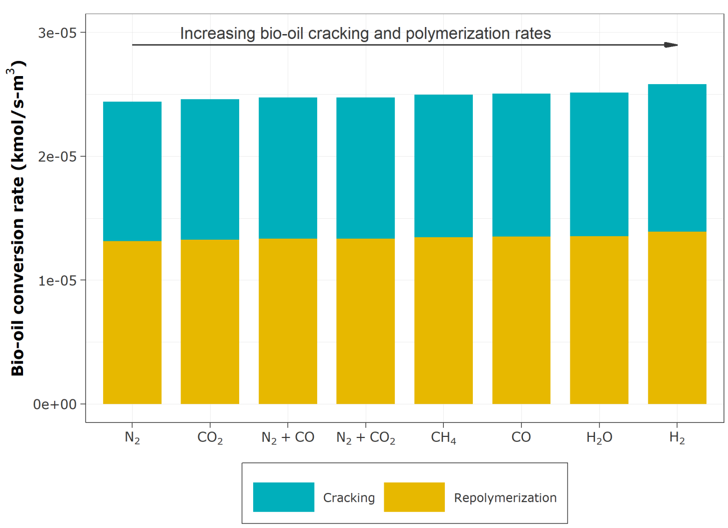

Figure 19: Time-average bio-oil cracking and polymerization rates.

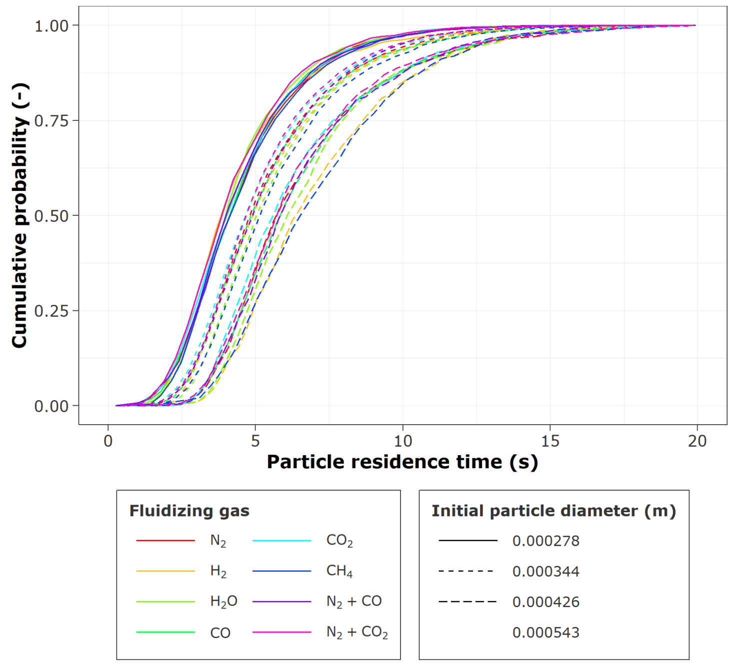

Figure 20: Cumulative particle residence time distribution as affected by fluidizing gas and initial particle diameter.

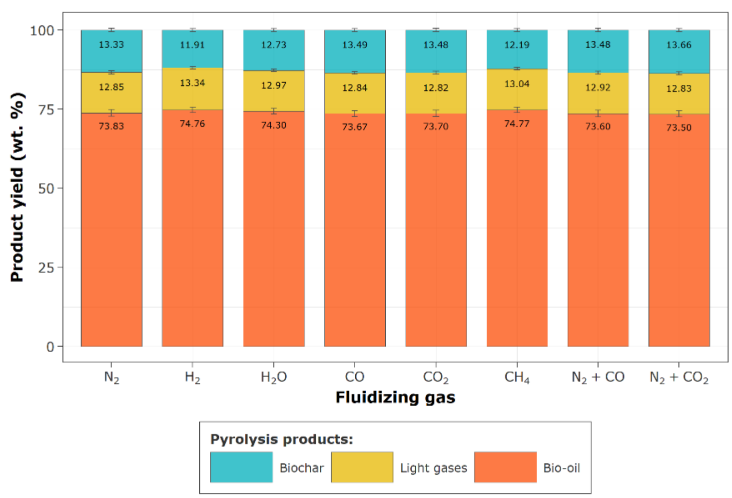

Figure 21: Pyrolysis product distribution as affected by fluidizing gas. Product yields are calculated on a biomass basis.

6 Conclusion

Gas effects in a fluidized bed biomass pyrolysis reactor using engineering correlations, low-order models, and CFD simulations were investigated for N2, H2, H2O, CO, CO2, and CH4 carrier gas mixtures. Our findings reveal viscosity of a gas mixture can be significantly underestimated depending on the model. Also, fluidization characteristics such as U_{mf} are greatly affected by gas properties but the effect on biomass pyrolysis yields is negligible.

7 Source code

Python models used to generate results for this article are available on the CCPC GitHub at `https://github.com/ccpcode/gas-effects-bfb`. Functionality provided by the Chemics package was used for gas properties and various fluidization calculations. More information about Chemics is available at `https://chemics.github.io`.

References

[1] M. Asadullah et al. "Jute stick pyrolysis for bio-oil production in fluidized bed reactor". In: *Bioresource Technology* 99 (2008), pp. 44–50.

[2] Colomba Di Blasi. "Analysis of Convection and Secondary Reaction Effects Within Porous Solid Fuels Undergoing Pyrolysis". In: *Combustion Science and Technology* 90 (1993), pp. 315–340.

[3] Colomba Di Blasi and Carmen Branca. "Kinetics of Primary Product Formation from Wood Pyrolysis". In: *Industrial & Engineering Chemistry Research* 40 (2001), pp. 5547–5556.

[4] A.V. Bridgwater. "Principles and practice of biomass fast pyrolysis processes for liquids". In: *Journal of Analytical and Applied Pyrolysis* 51 (1999), pp. 3–22.

[5] Tony Bridgwater. "Challenges and Opportunities in Fast Pyrolysis of Biomass: Part I". In: *Johnson Matthey Technology Review* 62.1 (2018), pp. 118–130.

[6] Richard S. Brokaw. *Viscosity of Gas Mixtures*. NASA Technical Note NASA-TN-D-4496. NASA Lewis Research Center, 1968.

[7] A.P. Collier et al. "The heat transfer coefficient between a particle and a bed (packed or fluidised) of much larger particles". In: *Chemical Engineering Science* 59.21 (2004), pp. 4613–4620.

[8] Thomas A. Davidson. *A Simple and Accurate Method for Calculating Viscosity of Gaseous Mixtures*. Tech. rep. Report of Investigations 9456. United States Department of the Interior, 1993.

[9] Gary H. Ganser. “A rational approach to drag prediction of spherical and nonspherical particles”. In: *Powder Technology* 77.2 (1993), pp. 143–152. DOI: `https://doi.org/10.1016/0032-5910(93)80051-B`. URL: `http://www.sciencedirect.com/science/article/pii/003259109380051B`.

[10] Xi Gao et al. “Development and validation of an enhanced filtered drag model for simulating gas-solid fluidization of Geldart A particles in all flow regimes”. In: *Chemical Engineering Science* 184 (2018), pp. 33–51. DOI: `https://doi.org/10.1016/j.ces.2018.03.038`. URL: `http://www.sciencedirect.com/science/article/pii/S0009250918301726`.

[11] Dimitri Gidaspow. *Multiphase Flow and Fluidization: Continuum and Kinetic Theory Descriptions*. Academic Press, Inc., 1994.

[12] Thomas Graham. “On the Motion of Gases”. In: *Philosophical Transactions of the Royal Society of London* 136 (1846), pp. 573–631.

[13] F. Herning and L. Zipperer. “Calculation of the Viscosity of Technical Gas Mixtures From the Viscosity of the Individual Gases”. In: *Gas-und Wasserfac* 79 (1936), pp. 69–73.

[14] Daniel Howe et al. “Field-to-Fuel Performance Testing of Lignocellulosic Feedstocks: An Integrated Study of the Fast Pyrolysis-Hydrotreating Pathway”. In: *Energy & Fuels* 29 (2015), pp. 3188–3197.

[15] Kwang Ho Kim, Robert C. Brown, and Xianglan Bai. “Partial oxidative pyrolysis of acid infused red oak using a fluidized bed reactor to produce sugar rich bio-oil”. In: *Fuel* 130 (2014), pp. 135–141.

[16] Daizo Kunii and Octave Levenspiel. *Fluidization Engineering*. 2nd ed. Chemical Engineering. Butterworth-Heinemann, 1991.

[17] Liqiang Lu et al. “EMMS-based discrete particle method (EMMS–DPM) for simulation of gas–solid flows”. In: *Chemical Engineering Science* 120 (2014), pp. 67–87. DOI: `https://doi.org/10.1016/j.ces.2014.08.004`. URL: `http://www.sciencedirect.com/science/article/pii/S0009250914004229`.

[18] Ofei D. Mante et al. “The influence of recycling non-condensable gases in the fractional catalytic pyrolysis of biomass”. In: *Bioresource Technology* 111 (2012), pp. 482–490.

[19] Pelle Mellin, Efthymios Kantarelis, and Weihong Yang. “Computational fluid dynamics modeling of biomass fast pyrolysis in a fluidized bed reactor, using a comprehensive chemistry scheme”. In: *Fuel* 117 (2014), pp. 704–715.

[20] Dinesh Mohan, Charles U. Pittman, and Philip H. Steele. “Pyrolysis of Wood/Biomass for Bio-oil: A Critical Review”. In: *Energy & Fuels* 20 (2006), pp. 848–889.

[21] Charles A. Mullen, Akwasi A. Boateng, and Neil M. Goldberg. “Production of Deoxygenated Biomass Fast Pyrolysis Oils via Product Gas Recycling”. In: *Energy & Fuels* 27.7 (2013), pp. 3867–3874.

[22] Helio A. Navarro and Meire P. de Souza Braun. "Determination of the normal spring stiffness coefficient in the linear spring–dashpot contact model of discrete element method". In: *Powder Technology* 246 (2013), pp. 707–722. DOI: https://doi.org/10.1016/j.powtec.2013.05.049. URL: http://www.sciencedirect.com/science/article/pii/S0032591013004178.

[23] T.J.P. Oliveira, C.R. Cardoso, and C.H. Ataíde. "Bubbling fluidization of biomass and sand binary mixtures: Minimum fluidization velocity and particle segregation". In: *Chemical Engineering and Processing: Process Intensification* 72 (2013), pp. 113–121. DOI: https://doi.org/10.1016/j.cep.2013.06.010. URL: http://www.sciencedirect.com/science/article/pii/S025527011300158X.

[24] K. Papadikis, S. Gu, and A.V. Bridgwater. "Computational modelling of the impact of particle size to the heat transfer coefficient between biomass particles and a fluidised bed". In: *Fuel Processing Technology* 91 (2010), pp. 68–79.

[25] K. Papadikis et al. "Application of CFD to model fast pyrolysis of biomass". In: *Fuel Processing Technology* 90 (2009), pp. 504–512.

[26] Joseph P. Polin et al. "Conventional and autothermal pyrolysis of corn stover: Overcoming the processing challenges of high-ash agricultural residues". In: *Journal of Analytical and Applied Pyrolysis* 143 (2019), p. 104679.

[27] Joseph P. Polin et al. "Process intensification of biomass fast pyrolysis through autothermal operation of a fluidized bed reactor". In: *Applied Energy* 249 (2019), pp. 276–285.

[28] D.L. Pyle and C.A. Zaror. "Heat Transfer and Kinetics in the Low Temperature Pyrolysis of Solids". In: *Chemical Engineering Science* 39.1 (1984), pp. 147–158.

[29] Anna Trendewicz et al. "Evaluating the effect of potassium on cellulose pyrolysis reaction kinetics". In: *Biomass and Bioenergy* 74 (2015), pp. 15–25.

[30] C.R. Wilke. "A Viscosity Equation for Gas Mixtures". In: *The Journal of Chemical Physics* 18.4 (1950), pp. 517–519.

[31] Qingang Xiong et al. "Modeling the impact of bubbling bed hydrodynamics on tar yield and its fluctuations during biomass fast pyrolysis". In: *Fuel* 164 (2016), pp. 11–17.

[32] Q. Xue, T.J. Heindel, and R.O. Fox. "A CFD model for biomass fast pyrolysis in fluidized-bed reactors". In: *Chemical Engineering Science* 66.11 (2011), pp. 2440–2452.

[33] Carl L. Yaws. *Yaws' Critical Property Data for Chemical Engineers and Chemists*. Knovel, 2014.

[34] Huiyan Zhang et al. "Biomass fast pyrolysis in a fluidized bed reactor under N2, CO2, CO, CH4 and H2 atmospheres". In: *Bioresource Technology* 102 (2011), pp. 4258–4264.